Chinese Chemical Letters 35 (2024) 109657

Contents lists available at ScienceDirect

Chinese Chemical Letters

journal homepage: www.elsevier.com/locate/cclet

An AIE-based theranostic nanoplatform for enhanced colorectal cancer therapy: Real-time tumor-tracking and chemical-enhanced photodynamic therapy

Jia-Qi Feng[a,1], Xiang Tian[a,1], Rui-Ge Cao[b,c,1], Yong-Xiu Li[a], Wen-Long Liu[a], Rong Huang[b,*], Si-Yong Qin[a,*], Ai-Qing Zhang[a,*], Yin-Jia Cheng[a,*]

[a] Key Laboratory of Catalysis and Energy Materials Chemistry of Ministry of Education & Hubei Key Laboratory of Catalysis and Materials Science, School of Chemistry and Materials Science, South-Central Minzu University, Wuhan 430074, China
[b] School of Pharmaceutical Sciences, South-Central Minzu University, Wuhan 430074, China
[c] Institute of Animal Husbandry and Veterinary Science, Wuhan Academy of Agricultural Science and Technology, Wuhan 430208, China

ARTICLE INFO

Article history:
Received 2 January 2024
Revised 8 February 2024
Accepted 15 February 2024
Available online 20 February 2024

Keywords:
Photodynamic-chemotherapy
Co-assembly
AIE photosensitizer
Peptide drug
Theranostics

ABSTRACT

The combination of diagnostic and therapeutic agents in the form of theranostic platforms to enhance tumor therapeutic efficacy is receiving increasing attention in recent years. However, simultaneous encapsulation, embedding or conjugation of various agents to traditional theranostic nanocarriers always require intricate synthetic process. Herein, a supramolecular drug-drug self-delivery nanosystem (DSDN) based on a newly developed aggregation-induced emission (AIE) photosensitizer (CBTM) and an anti-tumor tyroservaltide (YSV) was constructed for near-infrared (NIR) fluorescence imaging-guided photodynamic/chemotherapy of tumor. Transmission electron microscopy (TEM) and dynamic light scattering (DLS) confirmed that YSV and CBTM could co-assemble into YSV/CBTM nanoparticles, with regular round-shape morphology and homogeneous size. Inspiringly, YSV/CBTM nanoparticles could effectively overcome the aggregation-caused quenching (ACQ) effect, and enter CT26 tumor cells with a high NIR fluorescence emission, allowing preoperative diagnosis. Meanwhile, the as-prepared YSV/CBTM could efficiently generate reactive oxygen species (ROS) under NIR light irradiation, exhibiting photodynamic ablation of tumor cells. More importantly, the peptide drug of YSV not only improved the availability of CBTM nanoparticles, but also served as a toxic adjuvant to enhance the photodynamic therapy (PDT) efficacy of CBTM. *In vitro* and *in vivo* assays revealed that most of colorectal tumor cells and tumor tissues were thoroughly ablated by photodynamic-chemotherapy integrated nanoparticles, resulting in longer survival of tumor-bearing mice. Regarding the advantages of the YSV/CBTM nanosystem, we believe this research could offer valuable guidance for the design of nanodrugs with high performance for cancer theranostics.

Colorectal cancer, one of most deadly cancer worldwide, has seriously threatened human health and life in recent decades [1]. Cancer diagnostics that enable early diagnosis and targeted therapy has attracted considerable attention in the advancement of metastatic colorectal cancer treatments [2,3]. As prior phototheranostics can perform simultaneous diagnosis and *in situ* photo-triggered therapy, it has emerged as a promising non-invasive therapeutic modality to surmount colorectal cancer. Among the numerous kinds of light-triggered theranostic trials, fluorescence imaging guided photodynamic therapy (PDT) has gained tremendous scientific research interests, due to its merits of high lesion-selectivity, therapeutic effectiveness, and diagnostic sensitivity [4]. In the noninvasive PDT process, light-activated photosensitizers primarily convert oxygen (O_2) into cytotoxic reactive oxygen species (ROS) through type I or type II photochemical reactions. As well-known, the abundant ROS produced by well-designed photosensitizers could induce significant tumor cell death and apoptosis, whereas the neighboring biological region remains unruined [5,6]. Currently, the photosensitizers derived from hematoporphyrin are considered as the first generation photosensitizers and widely used in cancer therapy [7,8]. Nevertheless, they tend to aggregate in the physiological environment and display weak or negligible visible light illumination with decreased ROS production [9,10]. This typical phenomenon, namely aggregation-caused quenching

* Corresponding authors.
E-mail addresses: ronghuang@mail.scuec.edu.cn (R. Huang), sy-qin@mail.scuec.edu.cn (S.-Y. Qin), 3074707@mail.scuec.edu.cn (A.-Q. Zhang), ChengYJ@mail.scuec.edu.cn (Y.-J. Cheng).
[1] These authors contributed equally to this work.

https://doi.org/10.1016/j.cclet.2024.109657
1001-8417/

(ACQ), always seriously impedes the practical applications of many conventional photosensitizers [11]. Aggregation-induced emission (AIE)-active photosensitizers with near-infrared (NIR) fluorescence emission enjoy advantages of profound emission efficiency and photosensitivity in the aggregation state, providing unprecedented opportunities in biomedical fields [12,13]. Furthermore, AIE photosensitizers are featured with less tissue scattering, negligible autofluorescence and deep-tissue penetration, resulting in fluorescence imaging-guided enhanced PDT [14]. However, the synthesis of red/NIR AIE agents is generally quite complicated and time-consuming. On the other hand, most of AIE photosensitizers suffer from poor water-solubility and insufficient biological stability, leading to unsatisfactory therapeutic outcomes. In order to address these bottlenecks, constructing an ideal drug delivery nanosystem *via* a facile and efficient strategy for high-performance NIR image-guided cancer treatment is very promising [15–17].

Taking these considerations into account, drug-drug self-delivery nanosystems (DSDNs) involving intracellular delivery of active drugs by themselves without extra nanocarriers, have paved the road for high performance tumor treatment [18]. Take full advantage of bottom-up approach, fabricated DSDNs usually hold the following attractions: (i) Customized nanostructures that avoid drugs from disruption and promote the selective drug accumulation in tumors *via* enhanced permeability and retention (EPR) effect; (ii) successfully avoid tedious fabrication procedures of additional nanocarriers; (iii) outstanding drug loading capacities (nearly to 100% for pure nanodrugs); and (iv) nearly no carrier-triggered systemic toxicity and immunogenicity. Among various kinds of anticancer drugs, peptide drugs have played important roles in cancer prevention and chemical treatment by virtue of their excellent bioactivity, biodegradability and mellow synthetic approach. The bioactive tyroservatide (YSV) is an ultra-small peptide drug that proves to exert low toxicity towards normal cells. However, YSV has been reported to suppress the cell cycle *via* inhibiting biological activity of histones and histone deacetylase in cancer cells, displaying superior chemotherapy (CT) for various kinds of cancers [19]. Unfortunately, peptide drug YSV is vulnerable to enzymatic digestion *in vivo*, which greatly hampers its clinical application. Excitingly, DSDN are constructed by drug-drug nanoconjugates or pure small molecule drugs *via* a self-assembly process, resulting in desirable drug delivery and controlled release profile.

In this contribution, as a proof of concept, we proposed a dual-drug co-assembly nanosystem (YSV/CBTM) for NIR fluorescence imaging-guided synergistic photodynamic/chemo cancer therapy (PDT/CT). As illustrated in Scheme 1A, YSV/CBTM was fabricated *via* the co-assembly of hydrophobic YSV and CBTM due to their intermolecular interactions, including π-π stacking and hydrogen bonding. After passive accumulation in tumors *via* EPR effects, YSV/CBTM displayed NIR-I fluorescence imaging and potent tumoricidal effects of combining CT and PDT, resulting in the remarkable image-guided chemo-photodynamic therapy (Scheme 1B). The molecular mass of YSV was characterized by ESI-MS (Fig. S1 in Supporting information). The synthetic route of the newly designed CBTM was shown in Scheme S1 (Supporting information), in which the Suzuki coupling reaction between 4-bromo-7-(2,2-dicyanovinyl)-2,1,3-benzothiadiazole and (4-(bis(4-methoxyphenyl)amino)phenyl)boronic acid with tetrakis(triphenylphosphine)palladium(0) as the catalyst and sodium carbonate as the base in toluene/water affords the target compound. In the skeleton of NIR-emissive AIE photosensitizer (CBTM), triphenylamine (TPA) was employed as the electron donor (D), benzothiadiazole containing electron-rich heteroatoms (S, N) was used as the electron acceptor (A), carbon-carbon double bond was introduced as the π-bridge (π), and two cyano units were utilized as the electron acceptor (A). The molecular structure of CBTM

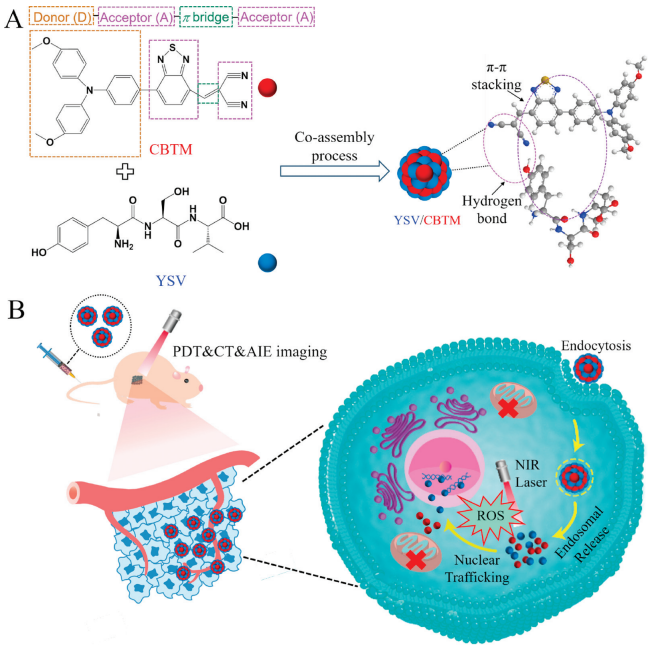

Scheme 1. Schematic illustration of construction of a multicomponent carrier-free DSNS (YSV/CBTM) for high performance AIE imaging-guided PDT/CT cancer therapy. (A) Synthesis route of YSV/CBTM nanomedicine. (B) Delivery of YSV/CBTM to the colorectal cancer cells *via* tail vein injection *in vivo*.

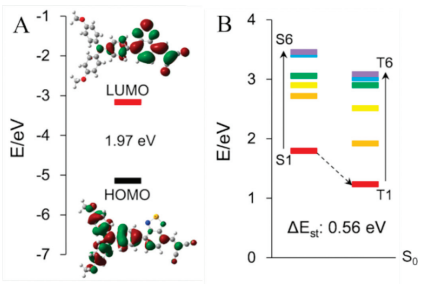

Fig. 1. HOMO-LUMO distribution by DFT calculations (A) and energy levels of S1–S6 and T1–T6 calculated by the vertical excitation of the optimized structure for CBTM (B).

was fully characterized by ^{1}H NMR (Fig. S2 in Supporting information) and MALDI-TOF mass spectrometry (Fig. S3 in Supporting information), confirming the successful fabrication of CBTM. The CBTM derived from an AIE-active TPA skeleton has a high tendency to show brighter fluorescence in the aggregated state, while the boosted push-pull effect and extended π-conjugation endow CBTM with emission to NIR-I region (630–1000 nm). To better understand the optical properties of AIE photosensitizer, density functional theory (DFT) calculations were performed using time-dependent B3LYP/6-31G(d) method. First, the frontier molecular orbitals of the CBTM with D-A-π-A structure show different distributions of the electron donor (D) and acceptor (A) motifs (Fig. 1). The highest occupied molecular orbital (HOMO) is predominantly distributed by TPA donor motif, while the lowest unoccupied molecular orbital (LUMO) is mainly localized on the electron-deficient benzothiadiazole and cyano groups, confirming the intramolecular charge transfer characteristics *via* electron excitation. As depicted in Fig. 1A, the HOMO-LUMO gap of CBTM was calculated to be 1.97 eV, which is smaller than that (2.63, 2.52, 2.60, 2.48 eV) of triphenylamine-based D-A type AIE molecules photosensitizers (TFN, MeO-TFN, Nap-TFN, Ant-TFN) at the same theoretical level [20]. It is widely accepted that the AIE process can be enhanced by reducing ΔE_{ST} between the lowest singlet (S1) and triplet (T1) excited states, thus

facilitating the intersystem crossing (ISC) process. Importantly, the ISC may trigger the spin crossover of triplet dioxygen ($^3O_2$) to produce reactive oxygen species (ROS) of $^1O_2$ and O^{2-}, $^{\bullet}OOH$, $^{\bullet}OH$, *etc*. Besides, the experimental ΔE_{ST} of CBTM was estimated to be 0.56 eV (Fig. 1B), indicating the favorable ISC process and ROS production in response to light irradiation. As well known, the narrow bandgap and strong intramolecular charge transfer (ICT) effect would benefit the long-wavelength NIR-I window of illuminators [21]. In order to verify the photoluminescence (PL) properties of CBTM in the aggregated state, the fluorescence intensity of CBTM in acetonitrile/water mixtures with different water volume fractions (0 to 95%) were investigated. As shown in Fig. S4 (Supporting information), CBTM exhibited extremely weak fluorescence emission in pure acetonitrile, which might be due to the free rotation of TPA phenyl rings in its molecularly dissolved state [22]. However, the PL signal of CBTM increased slightly by gradually increasing water volume fractions until 20%, ascribing to the strong ICT effect caused by the enhanced polarity of the mixture [23]. Further increasing water volume fractions, the PL intensity was boosted evidently. The fluorescence intensity of CBTM gradually increased to a maximum at 95% water fractions, which was 22 times higher than that in 10% of water fraction. It is clear that the existence of solvent effect and the restriction of intramolecular motion (RIM) mechanism are responsible for the above AIE phenomena of CBTM.

In order to increase the dispersibility of CBTM in aqueous medium, CBTM was processed into nanoparticles with biocompatible YSV peptide through antisolvent nanoprecipitation method. The antisolvent nanoprecipitation, a presentative bottom-up technique utilized to prepare drug nanoparticles, is easy to scale-up, cost effective and relatively simple [23,24]. In this work, the obtained YSV/CBTM nanoparticles were constructed at a YSV/CBTM weight ratio of 1:1. From the TEM image (Fig. S5A in Supporting information), it could be seen that the diameter of YSV/CBTM nanoparticles was around 140 nm. Besides, DLS observation (Fig. S5C in Supporting information) confirmed that the average hydrodynamic diameter of CBTM and YSV/CBTM nanoparticles was around 140 nm (polydispersity index (PDI): 0.12) and 154 nm (PDI: 0.17), respectively, which was slightly larger than that of TEM observation. This discrepancy could be explained by the brownian motion near the hydration layers at solid-liquid interfaces [25]. It is worth noting that the ultraviolet–visible (UV–vis) absorption spectrum of YSV/CBTM nanoparticles exhibited a broad peak centered at 270 nm corresponding to the benzyl rings of YSV (Fig. S5B in Supporting information). Specifically, the vibronic shoulder at 420 nm and 605 nm are ascribed to the π-π^* stacking structure of CBTM [26]. To further investigate the physicochemical stability of as-prepared formulations, DLS measurements were employed every day over a 7-day period. As shown in Figs. S5D and E (Supporting information), both CBTM and YSV/CBTM formulations remained stable in phosphate buffered saline (PBS) solution at 37 °C for one week, with no significant change in hydrodynamic size and PDI. These results demonstrated that CBTM and YSV/CBTM formulations possessed superior physicochemical stability in PBS. To better understand this phenomenon, the zeta potential of different nano-assemblies was also measured. Fig. S5F (Supporting information) demonstrated that zeta potential of CBTM, YSV, and YSV/CBTM nanoparticles was −14, −20, and −42 mV, respectively. These results indicated that the CBTM nano-assemblies carried negative charges and did not weaken the electrostatic repulsion among same-charged YSV when they are added to aqueous suspensions. Moreover, the electrostatic repulsive forces among CBTM and YSV/CBTM nano-assemblies were significant to prevent the aggregation and possess high colloid stability [27,28].

Despite the good stability of pure CBTM nanoparticles in PBS, we observed the violet precipitate at the inner wall of glass vial during the antisolvent nanoprecipitation (inset in Fig. S6B in Supporting information). Interestingly, this phenomenon was significantly mitigated after introducing YSV peptide to co-assemble with CBTM (inset in Fig. S6C in Supporting information), indicating an increase of CBTM availability in YSV/CBTM nanoparticle formulation. To further investigate the utilization efficiency of CBTM in as-prepared nano-assemblies, the CBTM precipitation from CBTM solution and YSV/CBTM solution were redissolved with THF solution under sonication, and the corresponding CBTM concentration was determined employing the standard calibration curve technique (Fig. S6A in Supporting information). As a consequence, the utilization efficiency of CBTM in pure CBTM nanoparticles was calculated to be 78% (Fig. S6B), while the utilization efficiency of CBTM in YSV/CBTM nano-assemblies was 95% (Fig. S6C). These results well demonstrated that the addition of soluble YSV peptide to CBTM could greatly elevate the aqueous solubility of YSV/CBTM.

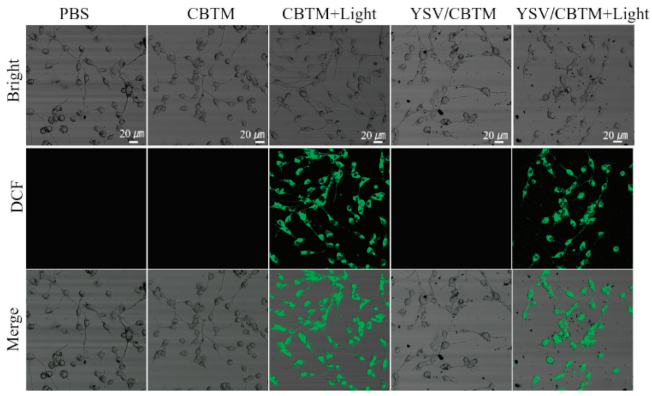

Fig. 2. Intracellular ROS generation of CBTM and YSV/CBTM observed by CLSM images in the absence/presence of 660 nm light irradiation (150 mW/cm^2) for 1 min. Scale bar: 20 μm.

To verify the potential photodynamic therapeutic function of CBTM upon photoexcitation, the ROS-generating property of CBTM and YSV/CBTM were validated in depth. Firstly, the $^1O_2$-specific probe singlet oxygen sensor green (SOSG) was employed to measure the ROS generation efficiency *via* PL spectroscopy [29]. Fore CBTM (40 μg/mL) and YSV/CBTM (the concentration of CBTM was 40 μg/mL), the emission profile of SOSG at 525 nm gradually elevated when increasing irradiation time, verifying the efficient generation of $^1O_2$ by CBTM (Fig. S7A in Supporting information) and YSV/CBTM (Fig. S7C in Supporting information) upon 660 nm light exposure (150 mW/cm^2). Contrarily, CBTM (Fig. S7B in Supporting information) and YSV/CBTM (Fig. S7D in Supporting information) exhibited negligible increase in the fluorescence intensity of SOSG at 525 nm, even after 30 min of incubation in dark. By virtue of the intrinsic singlet oxygen (type II ROS) generation ability of CBTM, YSV/CBTM could display the desirable physicochemical property and be exploited for efficient PDT of cancer.

Furthermore, a commercial ROS indicator 2,7-dichlorofluorescein diacetate (DCFH-DA probe) was employed to evaluate cellular ROS generation efficacy of the as-prepared CBTM and YSV/CBTM *via* green fluorescence imaging. As depicted in Fig. 2, both CBTM and YSV/CBTM presented remarkably enhanced green fluorescence of DCF in CT26 cells under 660 nm light irradiation (150 mW/cm^2 for 60 s), whereas no fluorescence was observed in the CBTM-treated group and YSV/CBTM-treated group without 660 nm laser irradiation. These results well demonstrated that CBTM and YSV/CBTM nano-assemblies could produce effective ROS generation under 660 nm laser irradiation.

The cellular uptake performance of CBTM and YSV/CBTM nano-assemblies were observed by confocal laser scanning microscopy (CLSM). After incubation with CBTM or YSV/CBTM nano-assemblies for 4 h, bright red fluorescence of CBTM was detected in CT26

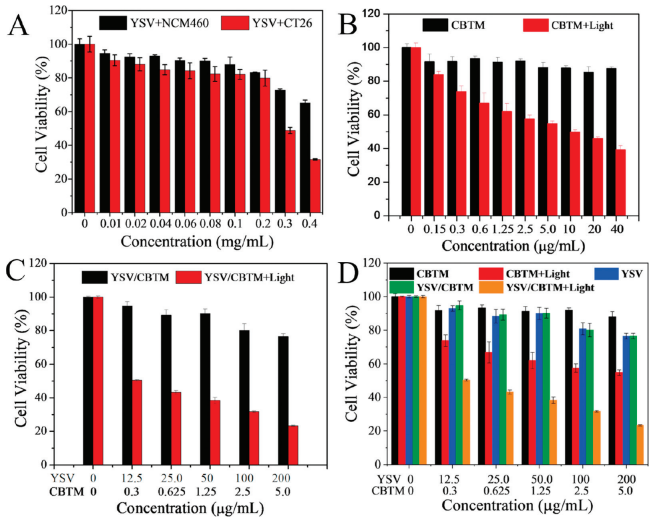

Fig. 3. *In vitro* toxicity. (A) Cell viability of CT26 cells and NCM460 cells after incubation with different concentration of YSV. Cell viability of CT26 cells after incubation with different concentration of CBTM (B) or YSV/CBTM (C) with/without 660 nm light irradiation (150 mW/cm^2). (D) Cell viability of CT26 cells after incubation with fixed concentrations of CBTM, YSV, and YSV/CBTM with/without 660 nm light irradiation (150 mW/cm^2, 3 min). The data were presented as the mean ± standard deviation (SD) ($n = 5$).

cells (Fig. S8 in Supporting information). Excitingly, the merged image indicated that the red fluorescence nanoparticles mainly located in tumor cells, proving the effective cell penetration and imaging ability of CBTM (Fig. S8A) and YSV/CBTM (Fig. S8B) nano-assemblies by CT26 cells. According to previous literatures, the EPR effect predominately depends on the surface properties, size of the nanocarriers, as well as the physiological properties of the tumors. Thus, nanoparticles with around 10–200 nm diameters could extravasate through the malformed tumor vessels easily, and accumulate at tumors due to the poor lymphatic drainage [30,31]. Hence, the suitable sizes of CBTM and YSV/CBTM nanoparticles would be very helpful for the optimal targeting and enhanced therapeutic effect of cancer treatment.

Inspired by efficient type II ROS generation and passive targeting capacity, *in vitro* toxicity of YSV, CBTM, and YSV/CBTM nano-assemblies against different cell lines were evaluated. Fig. 3A showed that YSV nano-assemblies could significantly inhibit the CT26 tumor cell viability in the high concentration range (0.2–0.4 mg/mL), whereas they exerted minimal toxicity towards normal NCM460 colonic epithelial cells.

Additionally, CBTM were nontoxic to CT26 cells in the absence of NIR light irradiation (Fig. 3B), suggesting the neglectable dark toxicity of CBTM nano-assemblies, which is a critical performance indicator of photosensitizers. Nevertheless, they displayed dose-dependent inhibitory effects of CT26 tumor cells in 48 h, under NIR laser irradiation (660 nm, 150 mW/cm^2) for only 3 min. Subsequently, the dark/photo toxicity of CT26 cells triggered by YSV/CBTM nano-assemblies were conducted (Fig. 3C). After 660 nm light irradiation, a significant reduce in the viability of CT26 cells occurred at an elevated YSV/CBTM concentration. Importantly, the half-inhibitory concentration (IC_{50}) of YSV/CBTM nanoparticles towards CT26 tumor cells under laser irradiation for combinatory therapy was found to be 12.8 μg/mL (Fig. 3D), while the IC_{50} for the PDT (Fig. 3B) and chemotherapy (Fig. 3A) alone was 20 μg/mL and 300 μg/mL, respectively. The above results verified the synergistic chemo-photodynamic therapy of YSV/CBTM.

Furthermore, the live/dead staining assays were launched to intuitively observe the apoptosis level of CT26 cells, after treatment of as-prepared YSV/CBTM nanoparticles. Living and dead CT26 cells were stained with calcein-AM (green) and PI (red), respectively [12]. As shown in Fig. S9 (Supporting information), a small amount of red fluorescence was detected in CT26 cells in the absence of NIR laser irradiation, verifying low toxicity of YSV/CBTM nanoparticles in the dark. Upon 660 nm laser irradiation (150 mW/cm^2) for 3 min, a concentration-dependent increase in the red fluorescence intensity were observed in YSV/CBTM-treated CT26 cells, demonstrating the remarkable cytotoxic effect towards tumor cells upon NIR light irradiation. The above results demonstrate that the constructed YSV/CBTM nano-assemblies provided effective accumulation for following enhanced PDT, which could significantly decrease side effect and injection frequency/dose of therapeutic agents for *in vivo* cancer therapy.

For the purpose of making sure that the observed cytotoxicity to CT26 cells was due to apoptosis, the annexin-FITC/PI double-staining assay was launched and analyzed by flow cytometry. As shown in Fig. S10 (Supporting information), After 8 h of co-cultivation, the YSV/CBTM (YSV concentration: 0.2 mg/mL) combined with light irradiation group (150 mW/cm^2, 3 min) exhibited a much stronger capacity to induce cell dead/apoptosis (73.8%) as compared with that of YSV/CBTM (YSV concentration: 0.01 mg/mL) under light irradiation (45.1%), YSV/CBTM (YSV concentration: 0.2 mg/mL) without light irradiation (22.2%), and YSV/CBTM (YSV concentration: 0.01 mg/mL) without light irradiation (11.2%). The above results confirmed that YSV/CBTM nanoparticles could induce concentration-dependent apoptosis in the presence of light irradiation.

Blood compatibility is an essential parameter of implanted materials in blood-contacting applications, which is also a crucial initial toxicity assay of biomaterials [32]. Hence, the hemolysis response and hemolysis rate of YSV, CBTM, and YSV/CBTM nanoparticles was investigated by measuring the lytic activity against rabbit red blood cells (RBCs). In terms of the standard ASTM-F765, a hemolysis rate of >5%, 2%–5%, or 0–2% is regarded to be hemolytic, slightly hemolytic, or non-hemolytic, respectively. As shown in Fig. S11A (Supporting information), YSV (200 μg/mL) and CBTM (5 μg/mL) exhibited a hemolysis rate of 2.0% and 2.3% in whole blood, indicative of slightly hemolysis. Nevertheless, when the concentration of YSV/CBTM solution reached up to 250 μg/mL, confirming no hemolysis. Furthermore, the hemolytic assay verified that no significant hemolysis was observed with the naked eye using YSV, CBTM, and YSV/CBTM (Fig. S11B in Supporting information). These results indicated that the fabricated YSV/CBTM nanoparticles possessed excellent blood compatibility and high safety during the blood circulation.

We employed an *in vivo* imaging system to evaluate the biological distribution of nano-assemblies (CBTM and YSV/CBTM) in CT26 tumor-bearing BALB/c female mice. All animal procedures were carried out by the South-Central Minzu University Guidelines for the Care and Use of Laboratory Animals and were approved by the South-Central Minzu University Animal Ethics Committee (SYXK (Wuhan) 2016-0089, No. 2021-SCUEC-AEC-033). After intravenous injection, the *in vivo* fluorescence signal was monitored at different time (0, 2, 4, 6, 8, 12 h). As expected, no fluorescence signals of CBTM were initially recorded at the tumor site in the mice. With the prolongation of the injection time of CBTM and YSV/CBTM, the fluorescence emission occurred at the injection site, and increased over time until peaking at 4 h (Fig. 4A). Besides, the mean fluorescence intensity (MFI) inside CT26 tumor cells demonstrated that both CBTM (Fig. 4B) and YSV/CBTM nano-assemblies (Fig. 4C) exhibited higher accumulation in tumor within 4 h. Subsequently, the fluorescence intensity decreased steadily from 4 h to 12 h. At 12 h, the NIR fluorescence in the CT26 tumor-bearing mice was very weak, owing to CBTM's quick elimination by the blood stream. Contrarily, YSV/CBTM nanoparticles maintained relatively higher fluorescence signals in tumor up to 12 h, confirming

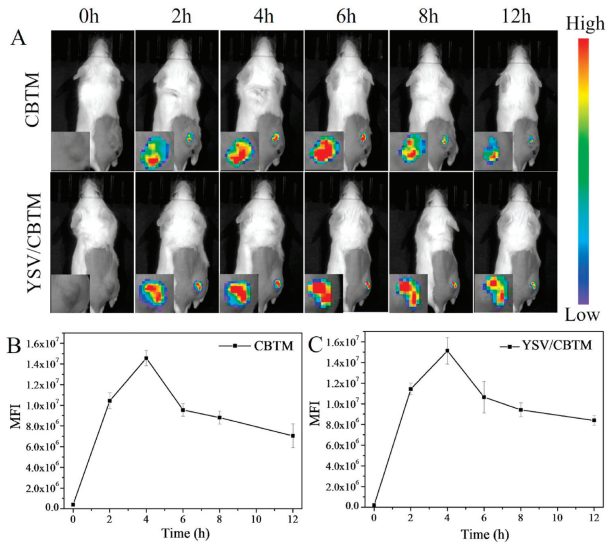

Fig. 4. (A) *In vivo* fluorescence imaging and biological distribution of CBTM and YSV/CBTM nanoparticles at different time (0, 2, 4, 6, 8, and 12 h) postinjection. The relative quantitative fluorescence intensity of CBTM (B) and YSV/CBTM nanoparticles (C) treated mice at different time (0, 2, 4, 6, 8, and 12 h) postinjection. The insets presented the magnified rectangular area. The data were presented as the mean ± SD ($n = 5$).

better retention of YSV/CBTM in the blood. The above results demonstrated that YSV/CBTM could specifically accumulated in the tumor sites for a long time. With the merit of tumor location, the YSV/CBTM nano-assemblies could significantly prompt PDT benefits, holding the potential for precise anti-cancer theranostics.

Encouraged by the impressive intracellular PDT/chemotherapeutic performance, YSV/CBTM was utilized as an idol theranostic agent for *in vivo* synergistic cancer therapy. Fig. 5A showed the schematic illustration of image-guided tumor treatment process. When the tumor volume reached 100 mm^3, the mice were randomly divided into five groups: PBS group, YSV plus Light group, CBTM plus Light, YSV/CBTM and YSV/CBTM plus Light group. As depicted in Figs. 5B and E, tumor growth was notably suppressed in YSV/CBTM plus light group compared with that in other groups. Additionally, the anti-tumor efficacy of each group was assessed by calculating the inhibition rate from the tumor weight. As shown in Fig. 5D, the tumor inhibition rate was 24.5% for CBTM, 27.9% for YSV, and 27.7% for YSV/CBTM nano-assemblies without light irradiation. However, YSV/CBTM exhibited a sharp increase in the tumor growth rate (average 62.5%) after 660 nm light illumination (1 W/cm^2, 5 min). These results demonstrated that YSV/CBTM held potent anti-tumor capability under 660 nm laser irradiation. We hypothesized that the superior therapeutic effect of YSV/CBTM against CT26 tumor in mice was mainly attributed to excellent tumor penetration, cellular membrane destruction, nuclear DNA dysfunction and eventually cell necroptosis. Notably, due to the fact that the dosages of free YSV, free CBTM, and YSV/CBTM were relatively small, the body weights of CT26 tumor-bearing mice in all five groups maintained steady in the early treatment course and elevated a little bit in the later stage, demonstrating the diminished systemic toxicity of as-prepared formulations (Fig. 5C).

Furthermore, the histological analysis was performed for post-treatment tumors. As shown in the hematoxylin and eosin (H&E) staining images (Fig. 5F), most of the tumor cells retained their normal morphology in PBS groups. However, the tumor cells were partially ruined and became necrotic for single CT-treated groups and single PDT-treated groups. What is more, the tumor cells in the YSV/CBTM group with NIR laser irradiation displayed extensive structural damage, indicative of significant apoptosis and necrosis. Similar phenomena were also verified by the TdT-mediated dUTP

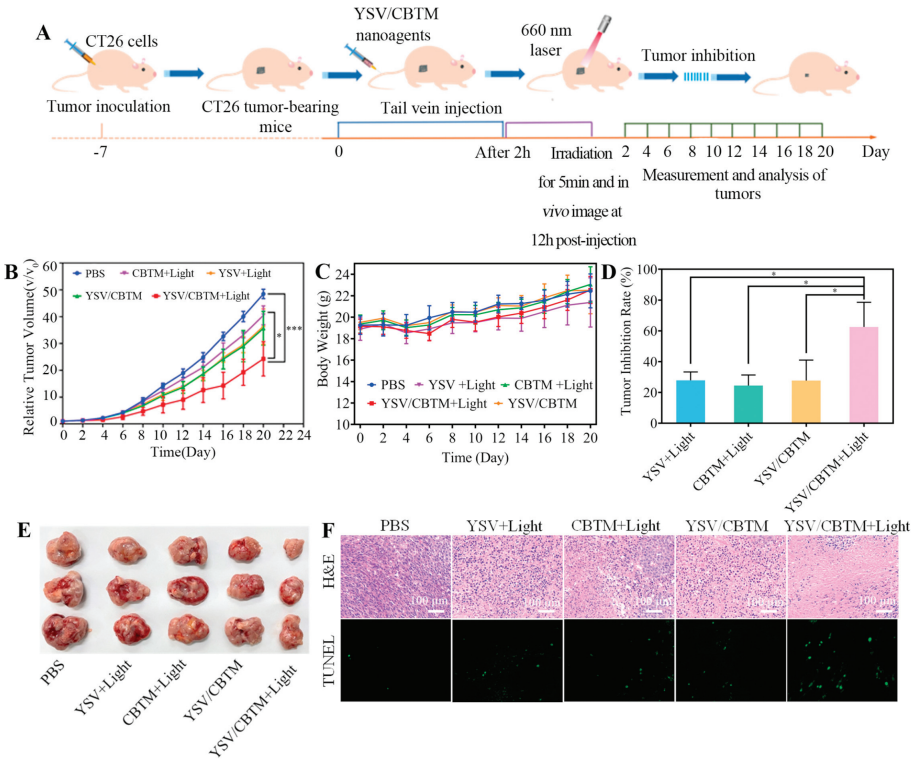

Fig. 5. *In vivo* therapeutic efficacy evaluation of PBS, YSV, CBTM, and YSV/CBTM in CT26 tumor bearing mice with/without 660 nm light irradiation (1 W/cm^2, 5 min). (A) Schematic illustration for the establishment of CT26 tumor xenograft models and the therapeutic process of CT26 tumors with YSV/CBTM. Relative tumor volume (B), relative body weight changes (C) and tumor inhibition ratio (D) for each group over the course of treatment. Tumor images (E), H&E staining and TUNEL of representative tumor tissues (F) for different groups after 21 days post-treatment. The data are shown as the mean ± SD ($n = 5$). Statistical significance was collected *via* one-way ANOVA with Tukey multiple comparison analysis. $^{*}P < 0.05$, $^{***}P < 0.001$. Scale bar: 100 μm.

nick-end labeling (TUNEL) assay. The YSV/CBTM plus light group displayed an evidently stronger green fluorescence of apoptotic cells. However, TUNEL-positive signals were almost undetectable in tumors receiving PBS, YSV, or CBTM plus NIR laser irradiation. Taken together, drug combinations (YSV/CBTM) were proved to display superior anti-tumor effect upon NIR laser irradiation.

Finally, the potential *in vivo* toxicity of different formulations was investigated by blood routine measurement and biochemical parameters. As shown in Fig. S12 (Supporting information), after tail vein injection of YSV, CBTM or YSV/CBTM with 660 nm light irradiation, white blood cell (WBC) (Fig. S12A), RBC (Fig. S12B), hemoglobin (HGB) (Fig. S12C), hematocrit (HCT) (Fig. S12D), mean corpuscular hemoglobin (MCH) (Fig. S12E), mean corpuscular hemoglobinconcentration (MCHC) (Fig. S12F), platelets (PLT) (Fig. S12G), and mean corpuscularvolume (MCV) (Fig. S12H) as the typical hematology index were tested. As a whole, there were no abnormal changes in monitored marker values for 7 days compared with PBS group after tail vein injection, suggesting that the as-prepared formulations (YSV, CBTM and YSV/CBTM) triggered negligible infection or inflammation in the treated mice. Besides, the hepatic-related function markers, such as alanine aminotransferase (ALT) (Fig. S12I) and aspartate aminotransferase (AST) (Fig. S12J), were examined in the blood biochemical tests, validating the negligible influence of YSV, CBTM and YSV/CBTM on the hepatic-related function markers. Thus, the YSV/CBTM treatment produced no significant negative influence on the blood chemistry as well as hepatic toxicity in the healthy mice, compared with PBS treatment for a long time.

H&E staining assays (Fig. S13 in Supporting information) of heart, liver, spleen, lung, and kidney have confirmed no significant abnormalities or lesions after YSV/CBTM treatment with or without NIR light irradiation. The above *in vivo* results confirmed that YSV/CBTM nanoparticles possessed satisfactory biocompatibility and few side effects in tumor theranostics.

In summary, we reported a versatile AIE-based theranostic nanoplatform (YSV/CBTM) to integrate NIR-I fluorescence, photodynamic, and chemotherapeutic effects for fluorescence imaging-guided synergistic cancer therapy. Through rational molecular design, uniform YSV/CBTM nanoparticles were formed *via* cooperative assembly of YSV and CBTM. The newly developed CBTM with D-A-π-A structure not only boosted the ICT efficacy for NIR fluorescence emission, but also effectively decreased ΔE_{ST} energy gap for significant ROS generation. Meanwhile, peptide drug YSV was responsible for potent tumoricidal effects, eventually boosted the phototherapeutic outcome of CBTM. Notably, after light treatment, YSV/CBTM displayed high degrees of CT26 cell death *in vitro*, and firmly retarded the proliferation of tumors together with tumor-specific bioimaging *in vivo*. Above all, this research not only provides a promising design strategy for exploring AIE photosensitizers with superior PDT performance, but also offers useful perspectives for constructing advanced theranostic nanosystems for effective clinical applications.

Declaration of competing interest

The authors declare that they have no known competing financial interests or personal relationships that could have appeared to influence the work reported in this paper.

Acknowledgments

This work was financially supported by Natural Science Foundation of China (Nos. 52173295, 52273313, 22377152, 52202357), the Fundamental Research Funds for the Central Universities, South-Central Minzu University (Nos. CZQ23036, CZY22005), and the Knowledge Innovation Program of Wuhan-Basic Research (No. 2023020201010150).

Supplementary materials

Supplementary material associated with this article can be found, in the online version, at doi:10.1016/j.cclet.2024.109657.

References

[1] Y.H. Zheng, X.R. You, S.Y. Guan, et al., Adv. Funct. Mater. 29 (2019) 1808646.
[2] K.Y. Ou, X.J. Xu, S.Y. Guan, et al., Adv. Funct. Mater. 30 (2020) 1907857.
[3] X.Y. Zhang, M.Y. Zhao, N. Cao, et al., Biomater. Sci. 8 (2020) 1885.
[4] J. Zhu, T. Xiao, J. Zhang, et al., ACS Nano 14 (2020) 11225.
[5] P. Wang, C. Liang, J. Zhu, et al., ACS Appl. Mater. Interfaces 11 (2019) 41140.
[6] J.W. Zhang, J.H. Yan, Y.N. Wang, et al., Chin. Chem. Lett. 35 (2024) 108434.
[7] T.C. Pham, V.N. Nguyen, Y. Choi, S. Lee, J. Yoon, Chem. Rev. 121 (2021) 13454.
[8] J.M. Chen, T.J. Fan, Z.J. Xie, et al., Biomaterials 237 (2020) 119827.
[9] F. Hu, S.D. Xu, B. Liu, Adv. Mater. 30 (2018) 1801350.
[10] Z.Y. Li, S. Chen, Y.R. Huang, et al., Chem. Eng. J. 450 (2022) 138087.
[11] Y. Hong, J.W.Y. Lam, B.Z. Tang, Chem. Commun. 29 (2009) 4332.
[12] J.B. Zhuang, B. Wang, H. Chen, et al., ACS Nano 17 (2023) 9110.
[13] C. Zhu, R.T.K. Kwok, J.W.Y. Lam, B.Z. Tang, ACS Appl. Bio Mater. 1 (2018) 1768.
[14] J. Dai, H.Y. Xue, D.G. Chen, et al., Coord. Chem. Rev. 464 (2022) 214552.
[15] X.R. You, L.Y. Wang, J.F. Zhang, et al., Chin. Chem. Lett. 34 (2023) 107720.
[16] Y. Zheng, Y. Liu, Z.C. Wu, et al., Adv. Mater. 35 (2023) 2210986.
[17] Z.D. Wang, C. Peng, Y. Zheng, et al., Adv. Funct. Mater. 33 (2023) 2214899.
[18] S.Y. Qin, J.Q. Feng, Y.J. Cheng, et al., Coord. Chem. Rev. 502 (2024) 215600.
[19] D. Wang, Z.H. Fan, H.F. Min, et al., Colloid. Surface. A 648 (2022) 129395.
[20] Q. Wang, C.B. Li, Y.C. Song, et al., Chem. Sci. 14 (2023) 684.
[21] X.L. Xu, G.J. Deng, Z.H. Sun, et al., Adv. Mater. 33 (2021) 2102322.
[22] Y. Yuan, S. Xu, C.J. Zhang, R. Zhang, B. Liu, J. Mater. Chem. B 4 (2016) 169.
[23] W.Z. Xu, Y. Chen, R.X. Yang, et al., ACS Nano 17 (2023) 18227.
[24] Z.H. Zhang, L.L. Shi, C.W. Wu, et al., ACS Appl. Mater. Interfaces 9 (2017) 29505.
[25] Y. He, Q.W. Chen, J.X. Yu, et al., J. Control. Release 359 (2023) 347.
[26] N. Somanathan, S. Radhakrishnan, Int. J. Mod. Phys. B 19 (2005) 4645.
[27] R. Jiang, J. Dai, X. Dong, et al., Adv. Mater. 33 (2021) 2101158.
[28] A. Verma, F. Stellacci, Small 6 (2010) 12.
[29] G. Grassi, C. Landi, C. Della Torre, et al., Environ. Sci. Nano 6 (2019) 2937.
[30] Y. Ding, Z. Tong, L. Jin, B. Ye, et al., Adv. Mater. 34 (2022) 2106388.
[31] C. He, Y. Hu, L. Yin, C. Tang, C. Yin, Biomaterials 31 (2010) 3657.
[32] H. Li, X. Zhang, X. Lin, et al., Mater. Chem. B 8 (2020) 1223.